Computers in Biology and Medicine 136 (2021) 104755

Contents lists available at ScienceDirect

Computers in Biology and Medicine

journal homepage: www.elsevier.com/locate/compbiomed

Personalized brachytherapy dose reconstruction using deep learning

Azadeh Akhavanallaf [a], Reza Mohammadi [b], Isaac Shiri [a], Yazdan Salimi [a], Hossein Arabi [a], Habib Zaidi [a,c,d,e,*]

[a] Division of Nuclear Medicine and Molecular Imaging, Geneva University Hospital, CH-1211, Geneva 4, Switzerland
[b] Department of Medical Physics, School of Medicine, Iran University of Medical Sciences, Tehran, Iran
[c] Geneva University Neurocenter, Geneva University, CH-1205, Geneva, Switzerland
[d] Department of Nuclear Medicine and Molecular Imaging, University of Groningen, University Medical Center Groningen, 9700 RB, Groningen, Netherlands
[e] Department of Nuclear Medicine, University of Southern Denmark, DK-500, Odense, Denmark

ARTICLE INFO

Keywords:
Brachytherapy
Dose reconstruction
Heterogeneity correction
Monte Carlo
Deep learning

ABSTRACT

Background and purpose: Accurate calculation of the absorbed dose delivered to the tumor and normal tissues improves treatment gain factor, which is the major advantage of brachytherapy over external radiation therapy. To address the simplifications of TG-43 assumptions that ignore the dosimetric impact of medium heterogeneities, we proposed a deep learning (DL)-based approach, which improves the accuracy while requiring a reasonable computation time.

Materials and methods: We developed a Monte Carlo (MC)-based personalized brachytherapy dosimetry simulator (*PBrDoseSim*), deployed to generate patient-specific dose distributions. A deep neural network (DNN) was trained to predict personalized dose distributions derived from MC simulations, serving as ground truth. The paired channel input used for the training is composed of dose distribution kernel in water medium along with the full-volumetric density maps obtained from CT images reflecting medium heterogeneity.

Results: The predicted single-dwell dose kernels were in good agreement with MC-based kernels serving as reference, achieving a mean relative absolute error (MRAE) and mean absolute error (MAE) of 1.16 ± 0.42% and 4.2 ± 2.7 × 10^{-4} (Gy.sec^{-1}/voxel), respectively. The MRAE of the dose volume histograms (DVHs) between the DNN and MC calculations in the clinical target volume were 1.8 ± 0.86%, 0.56 ± 0.56%, and 1.48 ± 0.72% for D90, V150, and V100, respectively. For bladder, sigmoid, and rectum, the MRAE of D5cc between the DNN and MC calculations were 2.7 ± 1.7%, 1.9 ± 1.3%, and 2.1 ± 1.7%, respectively.

Conclusion: The proposed DNN-based personalized brachytherapy dosimetry approach exhibited comparable performance to the MC method while overcoming the computational burden of MC calculations and over-simplifications of TG-43.

1. Introduction

Brachytherapy is a radiation therapy technique where radiation sources are located at small distances from the tumors, temporarily as in high-dose rate brachytherapy (HDR-BT) or permanently as in low-dose rate brachytherapy. In routine clinical practice, the dose distributions are commonly calculated using a simplified formalism proposed by the American Association of Physicists in Medicine (AAPM) Task Group No. 43 (TG-43) [1] or its updated version (TG-43U1) [2]. In these formalisms, the patient's anatomy is considered as a water-filled homogenous medium. A number of factors that influence the dose distributions, such as tissue and applicator heterogeneities, the finite geometry of the patient, the source-source and source-cable attenuation, and electron contributions to absorbed dose are ignored. Commercial treatment planning systems (TPSs), such as SagiPlan (Eckert & Ziegler BEBIG Co., Germany), attempted to address the limitations of TG-43 in attenuating media like a shield and metallic applicator through multiplication of the dose distribution obtained from the TG-43 model by an analytical attenuation factor. However, the effects of transmission angles and attenuation dependency on distance from the applicator in the region behind the shield (caused by multiple scattering) are ignored. A number of studies have addressed the limitations of TG-43 considered to cause an over/underestimation of the estimated planned dose and consequently treatment evaluation parameters for the clinical target volume

* Corresponding author. Geneva University Hospital, Division of Nuclear Medicine and Molecular Imaging, CH-1211, Geneva, Switzerland.
E-mail address: habib.zaidi@hcuge.ch (H. Zaidi).

https://doi.org/10.1016/j.compbiomed.2021.104755
Received 9 June 2021; Received in revised form 5 August 2021; Accepted 5 August 2021
Available online 8 August 2021

(CTV) and organs at risk (OARs) in different disease sites [3–12]. The AAPM published the recommendations of Task Group 186 on model-based dose calculation algorithms (MBDCAs) in brachytherapy beyond the TG-43 formalism [13]. They recommended the collapsed-cone [14], superposition/convolution [15], deterministic solutions using the linear Boltzmann transport equation [16] and Monte Carlo (MC) methods to improve the accuracy of dosimetric calculations in TPS [17]. In MBDCAs, the exact definition of source and applicator geometry inserted within the patient-specific computational model and heterogeneity corrections are implemented into the model [13]. For photon-emitting sources at energies lower than 150 KeV, the predominance of photoelectric interactions makes a large difference in energy absorption coefficients between different tissue types, which necessitates the introduction of heterogeneity corrections in dosimetry calculations. However, the dosimetric impact of tissue heterogeneities and finite patient dimensions for high-energy photon sources of Co-60 and Ir-192 in different treatment sites has been reported to be about 2% difference of dose-volume histogram (DVH) parameters between TG-43 against MC ground truth for the CTV, while these differences exceeded 5% for OARs [18]. Desbiens et al. studied the dosimetric impact of medium heterogeneities for Ir-192 in gynecologic HDR-BT using MC simulations [7]. They reported about 1% error on DVH-driven indices by taking into account tissue heterogeneities, whereas they reported that excluding the air pocket and applicator material from DVH calculation produces about 8.7% difference in CTV D90 with respect to TG-43.

Personalized dosimetry is required to improve clinical outcomes while lowering the risk of radiation-induced toxicity by growing recognition of precision medicine as a new paradigm aiming at increasing treatment efficacy. In this context, direct MC simulation is considered the gold standard for dosimetry calculations. However, its heavy computational burden and long execution time made it prohibitive for routine clinical application. More recently, the clinical adoption of deep learning (DL) has been extended into radiation oncology through treatment planning optimization [19–27]. A number of studies assessed knowledge-based automatic treatment planning using deep learning algorithms for external beam radiation therapy to overcome the computational burden of MC-based dose distribution for head and neck cancer patients [28–31]. In our previous work, we developed a framework for patient-specific internal dosimetry, where the core idea of the Medical Internal Radiation Dose Committee (MIRD) formalism was employed by training a physics-informed neural network to predict specific deposited energy kernels in a heterogeneous medium [32]. It has been shown that the deep learning-based model outperformed conventional MIRD approaches compared to reference MC simulation. We further extended our work to calcualte patient-specific dose distributions in brachytherapy. An independent work was simultaneously carried out by Mao et al. [33] on Ir-192-based HDR-BT dose prediction using deep learning. They designed a modified U-Net to predict the dose distribution considering contoured structures of patients, where 3D dose map obtained from MC simulations serving as ground truth. Considering the current literature, the main contributions of this work are (i) developing a physics-informed DL-based framework through feeding full voxel density map into the network (considering the presence of dense objects, such as metallic applicators, ovoid caps and air pockets); and (ii) introducing the volumetric dose map as a whole (taking into account attenuation/Compton scattering and their contribution to the overall absorbed dose).

In this work, we investigated the potential of predicting brachytherapy dose distributions using a 3D Deep Neural Network (DNN), wherein a two-channel input consists of a density map obtained from CT images along with the deposited energy kernel in water was fed into the network to predict patient-specific planned dose distributions.

2. Materials and Methods

2.1. Method description

In the first step, we developed a MC-based Personalized Brachytherapy Dosimetry Simulator (PBrDoseSim) wherein CT and DICOM-RT plan dataset are imported into the system to estimate patient-specific dose distribution. In the second step, we employed a DL model to generate personalized dose distributions from patient's CT images and treatment plans (Fig. 1). The DL network was designed as an image-to-image regression model to predict the specific energy deposition kernel when the radioactive source is located in the dwell position obtained from the treatment plan. The input data for the training is a two-paired channel composed of dose distribution kernel in water medium along with volumetric density maps. The corresponding output is a 3D dose distribution inspired from MC simulations. Given the input matrices, PBrDoseSim was employed to produce the dose distribution kernel for single-dwell sources considering the radioactive seed with unit activity located in the dwell position. The final dose distribution was reconstructed by superposition of single-dwell-position dose maps through dwell-time-weighted linear combination.

2.2. Data preparation

Data from 78 patients with locally-advanced cervical cancer treated with 3D conformal radiotherapy (45 Gy in 25 fractions) and HDR-BT (Co-60 source, 3/4 fractions and 8.6/7 Gy per fraction) as boost using a fletcher applicator were collected. A total of 2355 single-dwell positions (on average 30 dwell positions per patient) were obtained. Detailed patient demographics are given in Table 1. The original CT images (abdomino-pelvic coverage) with a resolution of $1 \times 1 \times 2$ mm^3 were resampled into 3 mm^3 resolution and CT Hounsfield Unit (HU) values converted to density map using a linear regression model [35]. We randomly divided our patient data into training (70) and external validation (8) datasets. Division by patient class was adopted to avoid sharing the patient geometry information between the training dataset and unseen external validation set.

2.3. Monte Carlo simulation

An in-house developed software for brachytherapy dose planning based on MCNP transport code was developed [34]. This program was implemented in Matlab and comprises four modules: i) geometry, ii) source definition, iii) simulation parameters, iv) output definition. The geometry module is fed by CT images. This module reads patient's CT images to provide a density map through the conversion of CT Hounsfield units (HUs) into different density classes [35]. In this module, the resolution size is a variable that can be modified by the user. Besides, the densities and corresponding material compositions assigned to each voxel are available to users for modification as an external library. The source module provides the definition of the source in MCNP code consisting of the seed model, particles and energy definition, as well as position and orientation of the source. The source geometry is defined using MCNP macrobodies according to the source design. The mode and source energy spectrum are defined based on the radioactive source material. The position and orientation of the seed is extracted from DICOM-RT data (seed orientation is defined based on the two end-to-end dwell positions). The simulation parameters include the number of histories tracked in the model and variance reduction techniques. The output module defines the parameters of the scored MCNP tally and the geometry of the output that can be fine-tuned by the user (Supplemental Table 1).

Dw representing the dose distribution in water was generated through the simulation of specified source seed in an infinite homogenous water medium. According to TG-43 formalism, heterogeneity correction of metallic applicator was applied on the planned dose by

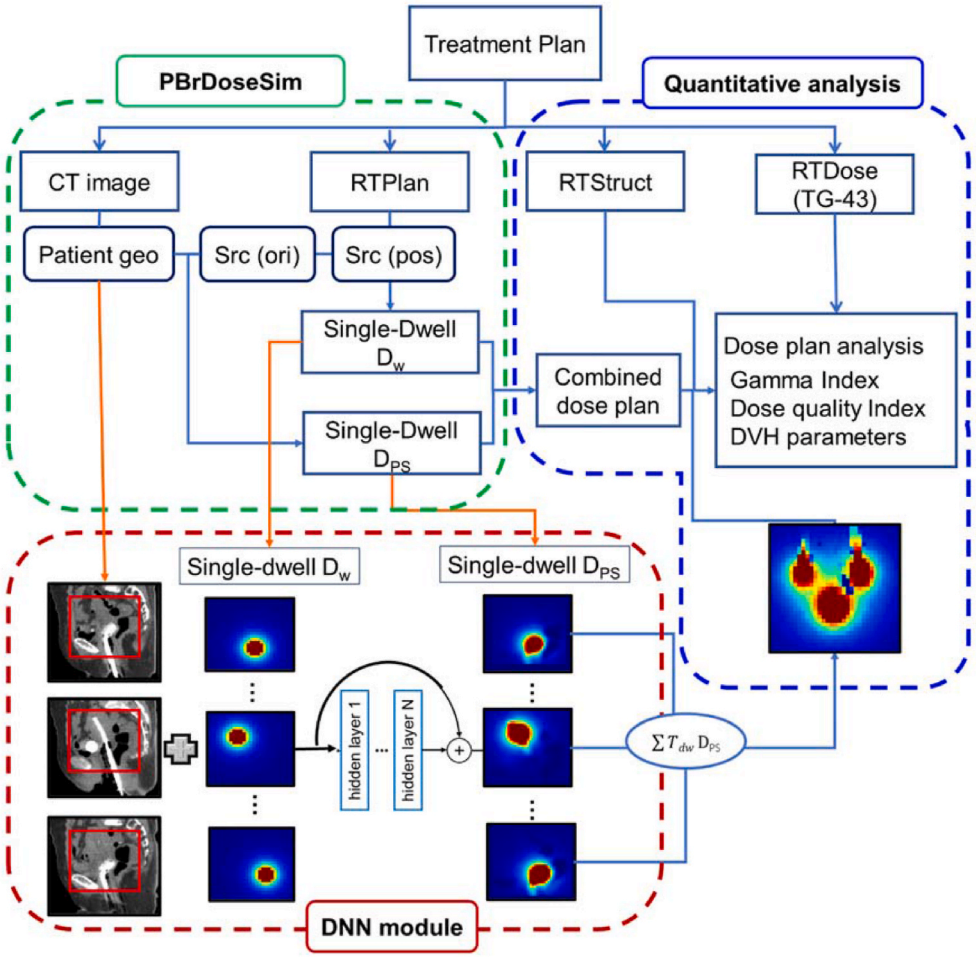

Fig. 1. Graphical abstract of the dose reconstruction procedure. The green panel shows the MC simulator structure, the red panel represents deep learning-based single-dwell dose kernel prediction, and the blue panel represents post-processing and analysis steps. D_w: single-dwell dose distribution in water, D_{PS}: single-dwell dose distribution in patient-specific geometry. geo: geometry, Src: source, pos: position, ori: orientation.

Table 1
Patients' demographic information.

Patients split	CTV_volume (cm^3)	Prescribed dose-D_{90} (Gy)	Dwell positions (#)			Dwell-pos Sparsity
			Ch. 1	Ch. 2	Ch. 3	
Training (No. 70)	21.94 ± 16.11	8.45 ± 0.85	7.4 ± 3.0	15.7 ± 5.0	6.95 ± 2.0	20.73 ± 3.84
Validation (No. 8)	20.22 ± 8.83	8.62 ± 0.86	7.3 ± 1.1	16.8 ± 3.6	7.7 ± 1.0	20.16 ± 3.32

Ch: applicator channel (Ch. 1: left oviod, Ch. 2: tandem and Ch. 3 right ovoid). Dwell-pos Sparsity: $\frac{1}{N}\sum_{N} r_{dwell-position} - \bar{r}$, N: total number of dwell positions.

multiplication of an attenuation factor depending on the applicator material and wall thickness.

In this work, density maps consisting of 13 density classes (air, lung, fat, soft tissue, and bone) where values above 100 HU were divided into eight discrete density groups. Afterward, the generated density maps were resampled to 3 mm^3 voxel size and were directly imported to the MCNP code, representing a heterogeneous medium of patient's anatomical structures. The material compositions were defined based on Schneider et al. [35]. BEBIG Co-60 HDR source (Model Co60.A86) used in this study was designed according to the company model (Supplemental Figure 1). The mode and energy spectrum of the emitted source particles was defined based on Co-60 (photons with two equal emission probability energy bins of 1.33 MeV and 1.17 MeV). The position and the source orientation were extracted from the DICOM-RT file and used as input to MCNP code considering the original coordinate in the TPS. Metal applicator (Fletcher tandem and oviods, Eckert & Ziegler BEBIG Co., Germany) segmented on CT images was modeled as foreign objects (density of 4.51 gr/cm^3) within the patients. 5 million (5×10^6) particles were tracked in these simulation sets and truncation methods, i.e., energy cut, were used as MCNP variance reduction techniques. Energy deposition mesh tally (type 3) was used in this simulation. 3D dose grids with a size of 34 × 34 × 34 voxels and a resolution of 3 mm^3 were designed to score voxelwise energy deposition. To benchmark our simulator, we designed a single dwell position treatment plan in a water sphere of 5 cm radius (Supplemental Table 2) and quantitatively analyzed the planned dose obtained from the TPS against our simulation.

2.4. Deep neural network architecture

In this work, a modified ResNet [45] architecture implemented on the TensorFlow platform was employed. The ResNet architecture consists of 20 cascaded convolutional layers with three levels of dilated residual blocks (Supplemental Figure 2). The first convolution layer is cascaded by three residual blocks with a 3 × 3 × 3 voxel convolution used to extract low-level features from the data. The next three residual blocks were designed to extract medium-level features using a dilation

convolution operation by a factor of 2, whereas the last three residual blocks capture high-level features by a dilation factor of 4. The network was trained to learn heterogeneity correction on D_w according to the information derived from density maps. The optimization of the network was defined based on L2 norm as objective function (OF) in addition to a regularization term of L1 in the following form:

$$OF(regularized) = \frac{1}{2}\sum (\hat{y} - y)^2 + \frac{\lambda}{2}\sum w \quad (1)$$

where $y, \hat{y}$ and λ are ground truth, prediction, and decay factor, respectively. w represents trainable parameters. The following setting was used for the training: optimizer = Adam, learning rate = 0.0001, batch size = 20, decay = 0.00001. Pairs of volumetric density maps representing medium heterogeneity and D_w reflecting the dose distribution around dwell position in homogenous medium as input, and corresponding patient-specific dose map (D_{ps}) as output were fed into the DNN. D_{ps} obtained from PBrDoseSim has a large dynamic range owing to the steep dose gradients with the distance to the source. Hence, it was non-linearly normalized for the sake of effective training of the network. Ten percent (10%) of the training dataset (a total of 220 single-dwell positions) was isolated for validation within the training of the model.

2.5. Evaluation strategy

Quantitative analysis of model performance was conducted by evaluating the mean relative absolute error (MRAE), voxelwise mean absolute error (MAE), and kernelwise absolute mean error (AME) between DNN and MC-based single-dwell dose maps. Furthermore, dose distribution quality metrics, i.e. 3D Gamma analysis for multiple criteria (1%/3% dose deviation (DD), 3 mm distance-to-agreement (DTA), total plan volume/100% isodose volumes), conformity index (COIN), dose homogeneity index (DHI), dose non-uniformity ratio (DNR), and dose-volume histogram (DVH) parameters were investigated as clinically relevant indices. Two groups of indicators consisting of CTV-based indices and OAR-based indices were defined. D_{xx} is the absorbed dose received by xx % of the target volume, whereas V_{xx} is the percentage of the target volume receiving at least xx % of the prescribed dose. D_{xcc} represents the minimum dose received by x cm^3 of an OAR. The distribution of the results was analyzed using Kolmogorov–Smirnov test where multiple comparisons between different methods against the standard of reference was analyzed using Dunnet post-hoc-test ($p < 0.05$).

3. Results

The details of PBrDoseSim evaluation in water phantom are summarized in Supplemental C. A single-dwell dose kernel and combined dose distribution along with axial dose profiles are illustrated in Fig. 2, where the relative difference between the two profiles are about 0.8% and 1.59%, respectively. The MRAE in a 10 × 10 × 10 window around the dwell position ($MRAE_c$) was calculated owing to the large contribution of absorbed doses in proximity to the source position, yielding 1.16 ± 0.42% difference between DNN and MC results.

3.1. Clinical studies

Dose quality indices obtained from MC simulation through the whole dataset are illustrated in Fig. 3. The average value (95% Confidence Interval (CI95%)) of COIN, DNR and DHI indices were calculated as 0.24 (0.15), 0.65 (0.15), and 0.34 (0.15), respectively. The DNN outperformed other approaches by achieving the lowest bias (0.05%) and the smallest variance (0.48%) against MC calculations. Voxelwise gamma analysis in the form of cumulated volume histogram of predicted DNN-based dose distribution compared to MC-based dose map for multiple criteria of all studied cases are presented in Fig. 3 (bottom). This graph confirms the gamma passing rate (Gamma-value<1) of about 99.9% for all analyzed criteria.

The predicted DNN-based DVH shows a consistent shape with those obtained from the MC method serving as reference (Fig. 4). The mean relative absolute error of DVH-driven dose metrics between DNN and D_w

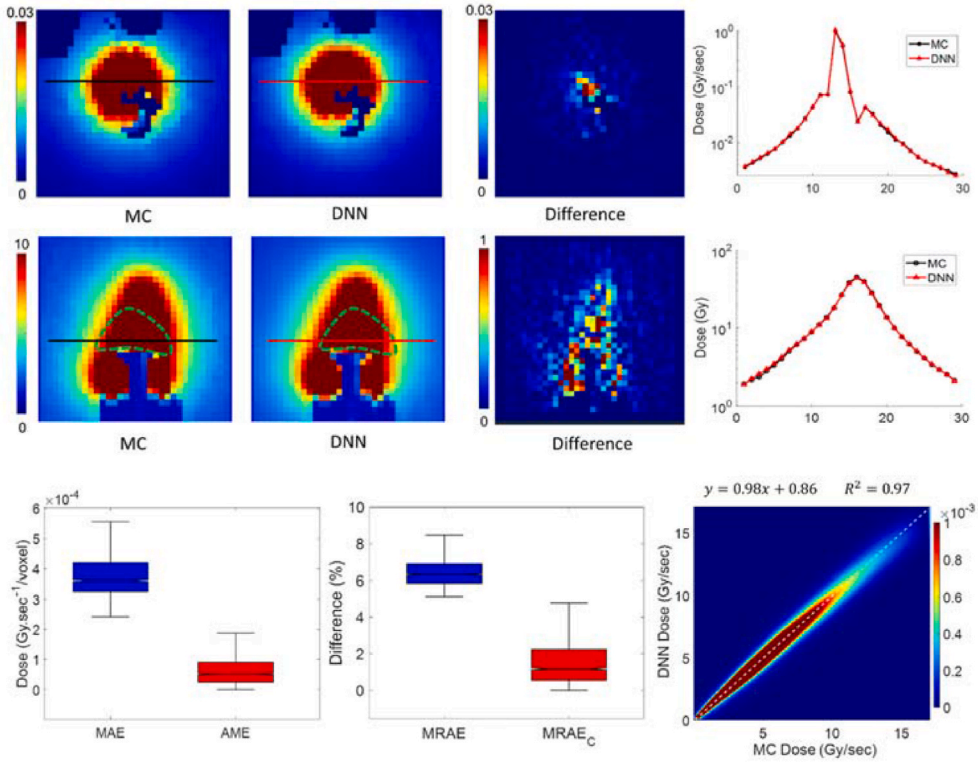

Fig. 2. Single-dwell dose kernel (axial view, top panel) and combined dose map (pear-shaped dose distribution, coronal view, middle panel) obtained from MC simulations and DNN model along with bias map in absolute unit of Gy and line profiles across the kernels. Comparison of MAE and AME (bottom left), MRAE (%) and $MRAE_C$ (%) (bottom middle) obtained within planned dose when using DNN against MC-based approaches. Joint histogram analysis displaying the correlation between the local voxels between predicted dose maps against their corresponding MC-based ground truth (bottom right).

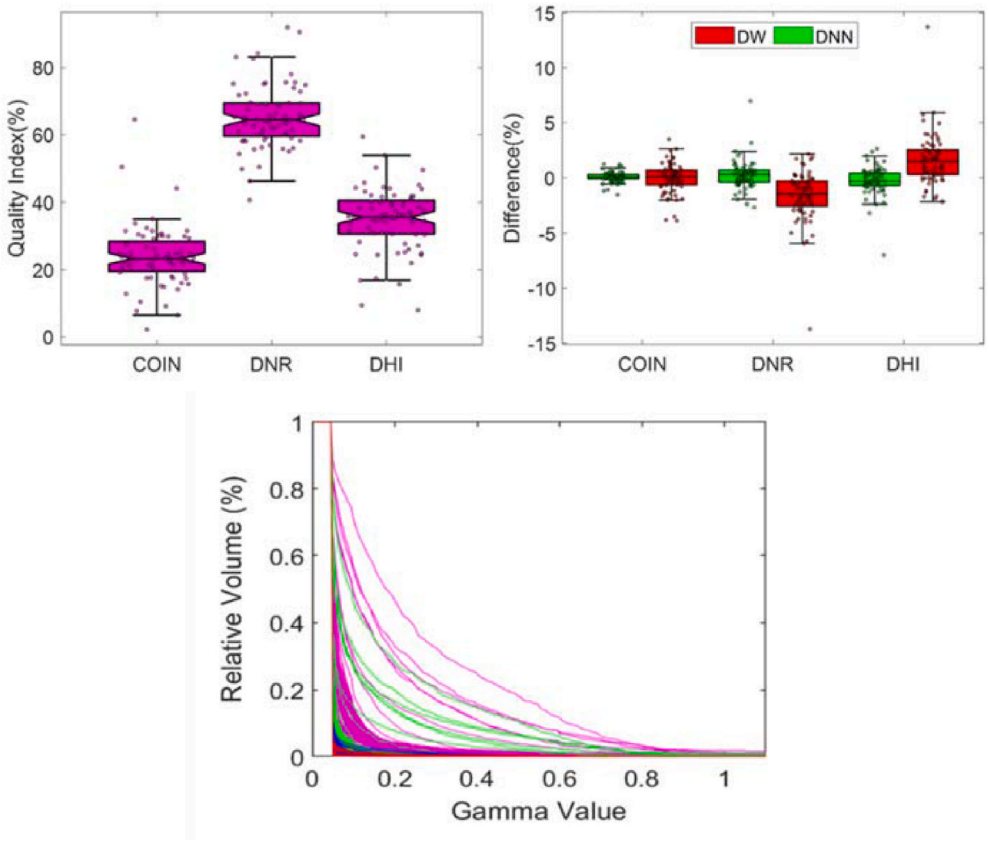

Fig. 3. Dose quality metrics of the whole dataset according to the dose distribution obtained from MC-based calculations (top left) along with the differences between quality indices calculated by DNN and Dw models against MC ground truth (top right). Cumulated volume histogram of gamma analysis between dose maps obtained from DNN with respect to MC-based dose distributions for 100%isodose volumes, (1% and 3%) DD, 3 mm DTA, [coded as 100%isodose, (1% and 3%), 3 mm] and total dose volumes, (1% and 3%) DD, 3 mm DTA, [coded as total, (1% and 3%), 3 mm] (bottom).

approach with respect to MC-based results were 1.4 ± 0.9% and 2.4 ± 2.1, respectively. While for volumetric metrics, these were 1.05 ± 1.18% and 2.1 ± 3.2%, respectively. In the current cervical patient dataset, three organs were delineated as OARs (sigmoid, bladder, and rectum) where D_{5cc} and D_{2cc} metrics are shown in Fig. 5. The mean relative absolute error of DVH parameters in OAR regions between DNN and D_w compared to MC simulations resulted in 1.6 ± 1.6% and 8.7 ± 14.94%, respectively. According to Kolmogorov–Smirnov test on the current dataset, non-parametric statistical analysis was utilized. The post-hoc comparison confirms that the differences between DVH-driven metrics obtained from DNN (*p-value* = 0.99) and D_w (*p-value* = 0.68) with respect to those from MC-based approach are not statistically significant.

3D gamma analysis for the unseen external validation set is illustrated in Fig. 6, which compares the predicted DNN-based dose distribution against MC-based dose map for multiple criteria, namely 1%/3% DD in 3 mm DTA and local normalization, for both total dose distribution volume and 100% isodose volume. The cumulated volume histogram depicts the gamma passing rate (Gamma-value<1) of 99.9% for all analyzing criteria. Furthermore, the maximum intensity projection of 3D gamma maps of validation dataset are shown in Supplemental Figure 5. Quality indices obtained from DNN and D_w dose distributions are depicted along with MC-based as ground truth (Fig. 6). The MRAE of COIN and DNR indices between DNN models compared to MC approach were 0.8 ± 0.5% and 1.8 ± 2.3% while these differences exceeded 0.8 ± 0.4% 3.4 ± 4.6% for D_w model compared to the reference.

The performance of the proposed DNN model on the external validation in terms of DVH-driven parameters are summarized in Tables 2–3. The MRAE of DVH metrics between DNN and MC was 1.5 ± 0.88%, 1.8 ± 0.86%, 1.3 ± 1%, 0.85 ± 0.43%, 0.56 ± 0.56%, 1.48 ± 0.72%, 0.26 ± 0.38% for D95, D90, D50, V200, V150, V100 and V50 in the CTV region, respectively. Conversely, the D_w approach compared to MC yielded 2.45 ± 2%, 2.56 ± 1.4%, 3.9 ± 2.1%, 2.6 ± 2.5%, 2.9 ± 1.9%, 2.5 ± 1.6%, 0.37 ± 0.55% for the same metrics, respectively. For D2cc of the bladder, sigmoid, and rectum, the MRAE between DNN and MC method was 3.2 ± 1.9%, 2.4 ± 1.6%, 2.5 ± 2%, respectively. The post-hoc-test revealed no statistically significant differences between the metrics obtained from DNN with respect to the MC-based approach (*p*-value = 0.82). An intraclass correlation coefficient of 99.8% confirms that the results obtained from the proposed DNN method are in excellent agreement with MC serving as reference.

4. Discussion

Accurate calculation of the absorbed dose delivered to the tumor and specific surrounding OARs enables to maximize the treatment gain factor, which is the main advantage of brachytherapy over external beam radiotherapy. In this study, we developed a unified MC-based dosimetry platform enabling the transition from TG-43 to MBDCAs approach while covering the limitations of analytical models in MBDCA [36,37]. We designed a novel DNN architecture to solve a complex problem, i.e. Boltzmann transport equation, by translating the underlying fundamental physics of particle interactions into the computer vision domain.

We prepared a dataset of 78 cervical cancer patients from which only one treatment session was chosen to increase anatomical variabilities. The simulator was fed by with patient CT images and treatment plans providing patient-specific geometry and radioactive source position and orientation within the patient. 10 cm dose grid's size was selected based on the steep dose gradient with radial distance (inverse square law) [38] that covers the desired volume of interest for clinical dose evaluation. To confirm this assumption, isodose contours were calculated at the boundaries of selected dose grids for the whole dataset corresponding to 15% (±4%) of the prescribed dose. In addition, none of the evaluated metrics, i.e. DVH-driven indices were affected by this kernel size.

The predicted 3D dose kernels from DNN exhibited good agreement with MC serving as reference confirmed by joint histogram analysis

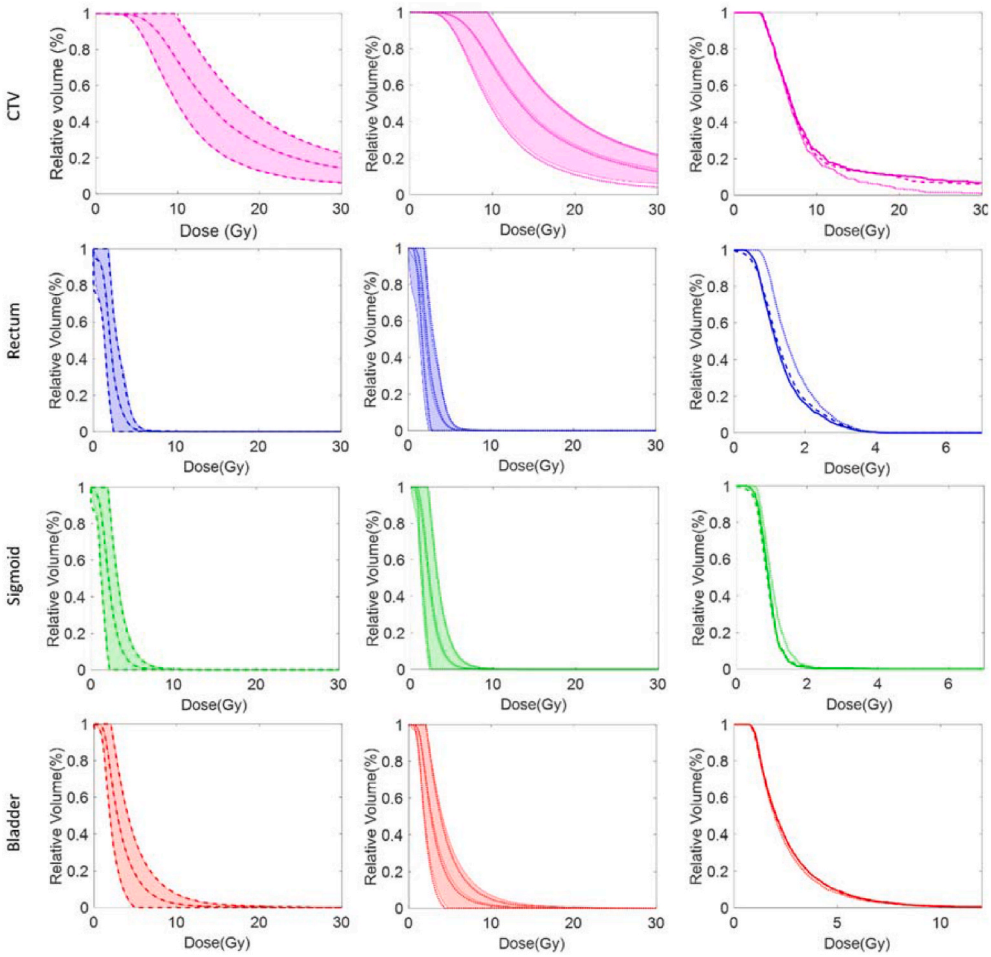

Fig. 4. Mean DVH plots along with CI95% (light shaded area) for the study population comparing the proposed DNN (left, dashed line), and Dw (middle, dotted line) plans against MC results (continuous line) are given for CTV (pink), rectum (blue), sigmoid (green) and bladder (red). DVH comparisons between DNN (dashed line) and Dw (dotted line) approach with respect to MC-based DVH (continuous line) are plotted for a randomly selected case study (right).

(Fig. 2). However, MRAE of 6.3% in the full planning volume can be attributed to the larger statistical uncertainty associated with MC simulations in far distances from the source. Voxel dose difference obtained from D_w model compared to MC was calculated with MRAE of about 13 ± 3% while $MRAE_c$ exceeds 31 ± 6% in the vicinity of dwell position (Supplemental Figure 4). Gamma analysis shows that at least 99.99% of points passed all criteria through the whole dataset (3 mm DTA was restricted by voxel size of the dose grids). In terms of DVH indices, DNN shows a comparable performance against MC calculations with an average relative bias of 0.7 (±1.4) % in the CTV volume. While, Dw showed an overall negative bias (−2.2%) and higher variance (3.34%) against MC results (Fig. 5). For OARs, the inserted balloon within the bladder caused a considerable underestimation of absorbed dose obtained from Dw, while DNN was trained to correct for its effect. For the sigmoid and rectum, there is low bias since OARs are almost composed of soft tissues and not located in the high dose regions, while the high variance is mainly caused by the presence of air pockets ignored in Dw models (low dose area in Fig. 4). External validation revealed good generalizability of the model with an average bias of 0.49 (±1.8)% in CTV dose indices with respect to the MC ground truth (details on case study interpretations are presented in Supplemental F). Mao et al. [33] reported the same magnitude of relative error (prostate: CTV D90 = 0.73%, OAR D2cc~1.1%; cervix: CTV D90 = 1.7%, OAR D2cc~ 2%) between their DL model against MC as ground truth using Ir-192. Although, they reported slightly less error for quantitative indices in their original model evaluation (prostate), they did not provide any evaluation on their full dose distribution compared to ground truth. Furthermore, they did not provide any baseline comparison, i.e. against Dw, thus, direct comparison of different models is not fair/insightful (owing to different dataset). One of the major limitations of their model is that it relies on contoured structures rather than original density map obtained from CT images. Therefore, it is unable to account for dense materials such as metallic applicator, ovoid caps, CT contrast agents, air pockets, etc, while our framework was based on a realistic physical model considering original voxel density maps as input. Furthermore, they used modified U-Net architecture composed of encoder-decoder (down and up sampling/polling layers) that converts original images to feature space by losing image resolution that would be issue in the presence of small heterogeneities. while in our proposed modified ResNet algorithm, image size is steady through all layers without losing image resolution. We modeled the fundamental principles of energy deposition through fully volumetric dose map rather than patchwise learning [39]. However, previous studies on Dl-based dose prediction did not explicitly incorporate compton scattering in their network and ignored its contribution to the overall dose distribution [33,40,41].

Overall, the DNN model outperformed TG-43-based approach in terms of heterogeneity correction in clinically relevant parameters of the HDR-BT planned dose. The required time for prediction of a combined dose (~30 dwell positions) was about 0.6 s (2080TI GPU, Xeon 2.30) compared to 540 min (10 core CPU, 64-GB RAM). This work bears some limitations that should be acknowledged. First, the choice of dose grid size/resolution and particle histories were restricted by the long simulation time and limited GPU memory for DL training process. Source position/orientation within the voxel is affected by course grid

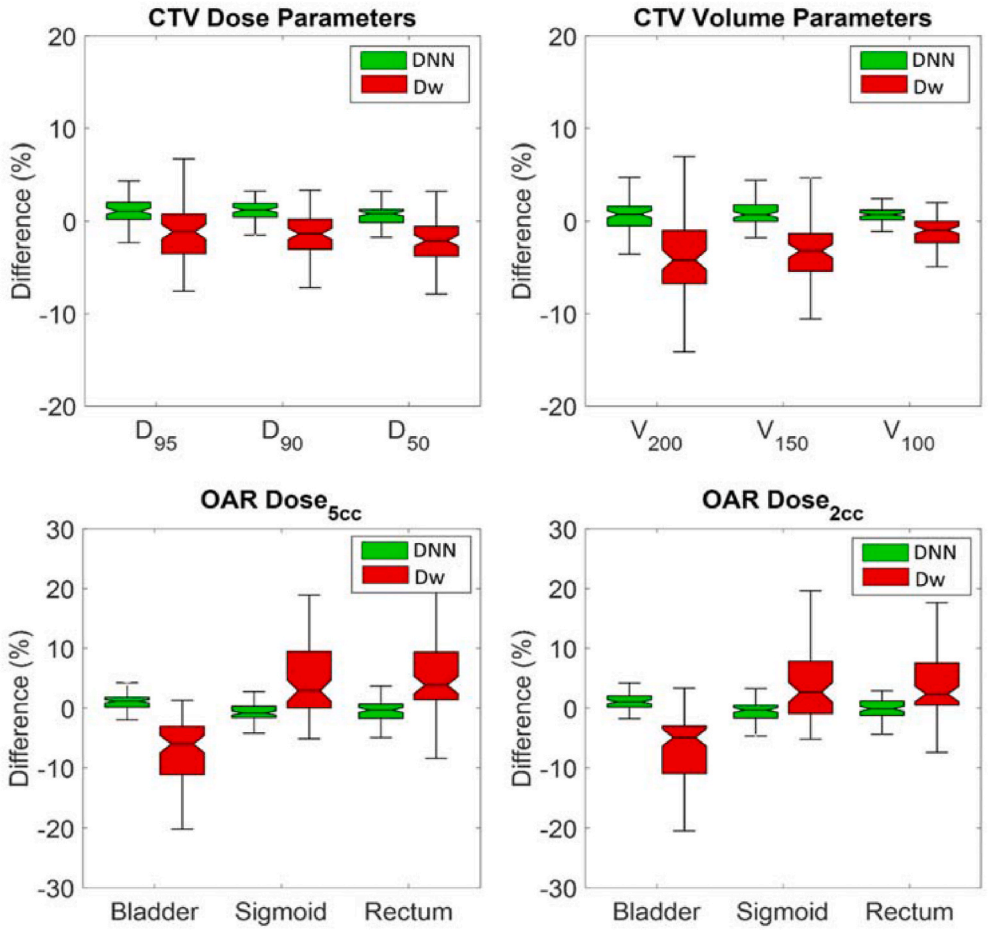

Fig. 5. Relative difference of DVH driven dose-volume indices between DNN and Dw method against MC-based approach for CTV (top) and OAR (bottom) for the studied population.

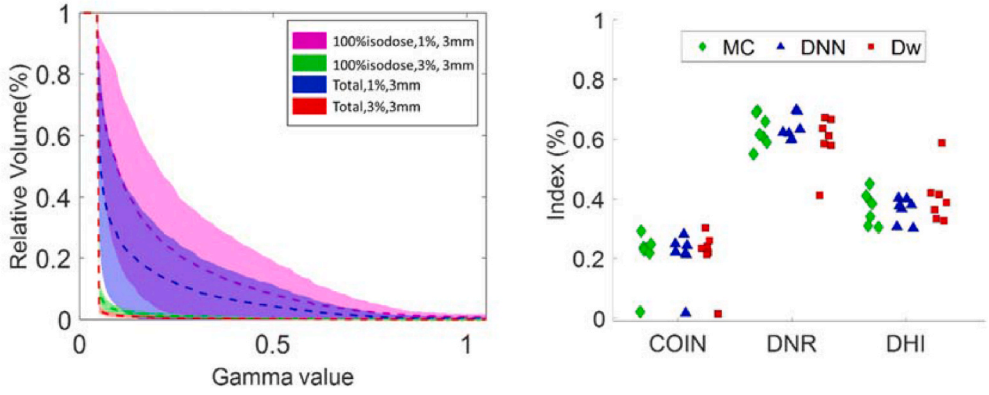

Fig. 6. Left panel: Mean gamma volume histogram (dashed) plots along with CI95% (light shade) for the external validation set comparing the proposed DNN model against MC-based dose distribution are given for 100% isodose volumes, (1% and 3%) DD, 3 mm DTA [coded as 100% isodose, (1% and 3%), 3 mm] and total dose volumes, (1% and 3%) DD, 3 mm DTA [coded as total, (1% and 3%), 3 mm]. Right panel: Quality indices calculated by MC, DNN and D_w models.

resolution, however, it has a local effect (first vicinity voxel) on deposited energy distribution and do not impact DVH-derived parameters. Second, the effect of the limited size of the training and validation dataset warrants further investigation. Third, we only provided a model for cervical HDR-BT using Co-60. Yet, this methodology is extendable to all types of brachytherapy treatments and different disease sites, where transfer learning can be exploited to obviate the need for a large ground truth dataset for model training.

It is worth highlighting the potential opportunities and challenges in the utilization of deep learning into brachytherapy personalized dose distributionning. In this context, DL algorithms can provide a solution for fast personalized dosimetry without compromising the accuracy. One of the challenges that DL can address is the construction of patient-specific computational models using structural images. It highly impacts the accuracy of MC-based dose calculation. Furthermore, it can be directly deployed for construction of planned dose for verification of clinical TG-43 dose distributions, inverse planning and treatment outcome prediction.

Table 2
Comparison between the proposed DNN and Dw models with respect to MC. The mean value of the DVH-driven dose metrics obtained from MC calculations are provided in absolute unit of Gy. The interquartile difference of dose indices in absolute unit of Gy and mean relative error in percent difference between DNN and Dw model against MC are presented for CTV and OARs.

ROI	DVH metrics	MC (Gy)	DNN vs. MC Diff (Gy)			D_w vs. MC Diff (Gy)			DNN_MC Diff ± std (%)	D_w_MC Diff ± std (%)
		(mean ± CI)	25%	50%	75%	25%	50%	75%		
CTV	D95	5.90 ± 1.6	−0.08	−0.04	0.07	−0.15	−0.06	0.02	−0.05 ± 1.86	−0.7 ± 3.3
	D90	6.69 ± 1.7	−0.14	−0.11	0.10	−0.19	−0.10	−0.06	−0.53 ± 2.11	−1.7 ± 2.5
	D50	12.12 ± 2.8	−0.20	−0.10	−0.02	−0.61	−0.46	−0.31	−0.90 ± 1.45	−3.9 ± 2.1
Bladder	D5cc	5.9 ± 1.4	−0.08	0.05	0.25	−0.63	−0.37	−0.12	1.61 ± 3	−5.93 ± 3.5
	D2cc	7.56 ± 1.66	−0.11	0.20	0.37	−0.54	−0.44	−0.20	1.92 ± 3.46	−5.91 ± 4.3
Sigmoid	D5cc	2.34 ± 1.36	−0.11	−0.04	0.01	−0.01	0.06	0.15	−1.43 ± 2	3.29 ± 6.5
	D2cc	2.94 ± 1.67	−0.11	−0.04	0.01	−0.01	0.14	0.21	−0.80 ± 3	4.23 ± 6
Rectum	D5cc	3.21 ± 0.53	−0.09	−0.04	0.00	0.04	0.09	0.15	−0.65 ± 2.87	2.87 ± 3.9
	D2cc	3.91 ± 0.61	−0.14	−0.03	0.03	−0.04	0.02	0.11	−1.32 ± 3.1	0.84 ± 3.3

Table 3
Mean value of the DVH-driven volume metrics obtained from MC calculations provided in absolute unit of cm^3 and relative percent of CTV volume. The interquartile difference of volume indices in (%) between the DNN and D_w models against MC is presented for the CTV.

ROI	DVH volume metrics	MC Reference (cm^3)	MC Reference (%)	DNN vs. MC (%)			D_w vs. MC (%)		
		(mean ± CI)	(mean ± CI)	25%	50%	75%	25%	50%	75%
CTV	V200	6.36 ± 3	30.8 ± 10.8	−0.83	−0.65	0.35	−3.71	−2.04	−0.81
	V150	9.73 ± 4.7	46.7 ± 16.3	−0.83	−0.27	0.00	−4.55	−2.78	−1.11
	V100	15.29 ± 7.5	72.7 ± 22.8	−1.63	−1.02	0.40	−3.72	−2.44	−0.77
	V50	19.81 ± 9.2	96.3 ± 8.5	−0.10	0.00	0.09	−0.24	0.00	0.19

5. Conclusion

We developed a unified pipeline for MC-based dosimetry in HDR-BT that has been used to provide an accurate set of MC simulations on a large retrospective cohort. We further developed a DNN model to provide an alternative solution for accurate personalized dose distributionning in brachytherapy to overcome the computational burden of MC simulations. The proposed algorithm achieved good agreement with MC calculations while outperforming the conventional TG-43-based formalism. Future work will focus on extending the core idea to different radioactive seeds for various disease sites.

Declaration of competing interest

All authors have participated in (a) conception and design, or analysis and interpretation of the data; (b) drafting the article or revising it critically for important intellectual content; and (c) approval of the final version.

The Article I have submitted to the journal for review is original, has been written by the stated authors and has not been published elsewhere.

The Images that I have submitted to the journal for review are original, was taken by the stated authors, and has not been published elsewhere.

This manuscript has not been submitted to, nor is under review at, another journal or other publishing venue.

The authors have no affiliation with any organization with a direct or indirect financial interest in the subject matter discussed in the manuscript.

Acknowledgements

This work was supported by the Swiss National Science Foundation under grant SNRF 320030_176052, the Private Foundation of Geneva University Hospitals under grant RC-06-01 and Iran's Ministry of Science.

Appendix A. Supplementary data

Supplementary data to this article can be found online at https://doi.org/10.1016/j.compbiomed.2021.104755.

References

[1] R. Nath, L.L. Anderson, G. Luxton, K.A. Weaver, J.F. Williamson, A.S. Meigooni, Dosimetry of interstitial brachytherapy sources: recommendations of the AAPM radiation therapy committee Task group No. 43. American association of Physicists in medicine, Med. Phys. 22 (1995) 209–234.
[2] M.J. Rivard, B.M. Coursey, L.A. DeWerd, W.F. Hanson, M.S. Huq, G.S. Ibbott, M. G. Mitch, R. Nath, J.F. Williamson, Update of AAPM Task Group No. 43 Report: a revised AAPM protocol for brachytherapy dose calculations, Med. Phys. 31 (2004) 633–674.
[3] J. Mason, B. Al-Qaisieh, P. Bownes, A. Henry, D. Thwaites, Investigation of interseed attenuation and tissue composition effects in (125)I seed implant prostate brachytherapy, Brachytherapy 13 (2014) 603–610.
[4] H. Afsharpour, J.P. Pignol, B. Keller, J.F. Carrier, B. Reniers, F. Verhaegen, L. Beaulieu, Influence of breast composition and interseed attenuation in dose calculations for post-implant assessment of permanent breast 103Pd seed implant, Phys. Med. Biol. 55 (2010) 4547–4561.
[5] G. Landry, B. Reniers, L. Murrer, L. Lutgens, E.B. Gurp, J.P. Pignol, B. Keller, L. Beaulieu, F. Verhaegen, Sensitivity of low energy brachytherapy Monte Carlo dose calculations to uncertainties in human tissue composition, Med. Phys. 37 (2010) 5188–5198.
[6] T. Brun, E. Torfeh, EP-1796: dosimetric comparison between TG43/TG186 algorithms and manual/inverse optimization in brachytherapy, Radiother. Oncol. 123 (2017) S986.
[7] M. Desbiens, M. D'Amours, H. Afsharpour, F. Verhaegen, M.C. Lavallée, I. Thibault, É. Vigneault, L. Beaulieu, Monte Carlo dosimetry of high dose rate gynecologic interstitial brachytherapy, Radiother. Oncol. 109 (2013) 425–429.
[8] K.A. Gifford, G.P. Fonseca, S. Thrower, F. Verhaegen, Comparison of two commercially available model based dose calculation algorithms and TG-43 for APBI brachytherapy, Brachytherapy 17 (2018) S32.
[9] D. Jacob, M. Lamberto, L. DeSouza Lawrence, F. Mourtada, Clinical transition to model-based dose calculation algorithm: a retrospective analysis of high-dose-rate tandem and ring brachytherapy of the cervix, Brachytherapy 16 (2017) 624–629.
[10] K. Zourari, T. Major, A. Herein, V. Peppa, C. Polgár, P. Papagiannis, A retrospective dosimetric comparison of TG43 and a commercially available MBDCA for an APBI brachytherapy patient cohort, Phys. Med. 31 (2015) 669–676.
[11] G. Anagnostopoulos, D. Baltas, E. Pantelis, P. Papagiannis, L. Sakelliou, The effect of patient inhomogeneities in oesophageal 192Ir HDR brachytherapy: a Monte Carlo and analytical dosimetry study, Phys. Med. Biol. 49 (2004) 2675–2685.
[12] E. Poon, J.F. Williamson, T. Vuong, F. Verhaegen, Patient-specific Monte Carlo dose calculations for high-dose-rate endorectal brachytherapy with shielded intracavitary applicator, Int. J. Radiat. Oncol. Biol. Phys. 72 (2008) 1259–1266.

[13] L. Beaulieu, A. Carlsson Tedgren, J.F. Carrier, S.D. Davis, F. Mourtada, M.J. Rivard, R.M. Thomson, F. Verhaegen, T.A. Wareing, J.F. Williamson, Report of the Task Group 186 on model-based dose calculation methods in brachytherapy beyond the TG-43 formalism: current status and recommendations for clinical implementation, Med. Phys. 39 (2012) 6208–6236.
[14] A. Ahnesjö, Collapsed cone convolution of radiant energy for photon dose calculation in heterogeneous media, Med. Phys. 16 (1989) 577–592.
[15] K. Zourari, E. Pantelis, A. Moutsatsos, L. Petrokokkinos, P. Karaiskos, L. Sakelliou, E. Georgiou, P. Papagiannis, Dosimetric accuracy of a deterministic radiation transport based 192Ir brachytherapy treatment planning system. Part I: single sources and bounded homogeneous geometries, Med. Phys. 37 (2010) 649–661.
[16] H. Hedtjärn, G.A. Carlsson, J.F. Williamson, Accelerated Monte Carlo based dose calculations for brachytherapy planning using correlated sampling, Phys. Med. Biol. 47 (2002) 351–376.
[17] D.W.O. Rogers, Fifty years of Monte Carlo simulations for medical physics, Phys. Med. Biol. 51 (2006) R287–R301.
[18] I. Fotina, K. Zourari, V. Lahanas, E. Pantelis, P. Papagiannis, A comparative assessment of inhomogeneity and finite patient dimension effects in (60)Co and (192)Ir high-dose-rate brachytherapy, J. Contemp. Brachytherapy 10 (2018) 73–84.
[19] H.H. Zhang, W.D. D'Souza, L. Shi, R.R. Meyer, Modeling plan-related clinical complications using machine learning tools in a multiplan IMRT framework, Int. J. Radiat. Oncol. Biol. Phys. 74 (2009) 1617–1626.
[20] L.V. van Dijk, L. Van den Bosch, P. Aljabar, D. Peressutti, S. Both, Roel.J.H. M. Steenbakkers, J.A. Langendijk, M.J. Gooding, C.L. Brouwer, Improving automatic delineation for head and neck organs at risk by Deep Learning Contouring, Radiother. Oncol. 142 (2020) 115–123.
[21] S. Kazemifar, A. Balagopal, D. Nguyen, S. McGuire, R. Hannan, S. Jiang, A. Owrangi, Segmentation of the prostate and organs at risk in male pelvic CT images using deep learning, Biomed. Phys. Eng. Exp. 4 (2018), 055003.
[22] Z. Zhu, E. Albadawy, A. Saha, J. Zhang, M.R. Harowicz, M.A. Mazurowski, Deep learning for identifying radiogenomic associations in breast cancer, Comput. Biol. Med. 109 (2019) 85–90.
[23] V.S. Parekh, M.A. Jacobs, Deep learning and radiomics in precision medicine, Expert Rev Precis Med Drug Dev 4 (2019) 59–72.
[24] Y. Peng, S. Chen, A. Qin, M. Chen, X. Gao, Y. Liu, J. Miao, H. Gu, C. Zhao, X. Deng, Z. Qi, Magnetic resonance-based synthetic computed tomography images generated using generative adversarial networks for nasopharyngeal carcinoma radiotherapy treatment planning, Radiother. Oncol. 150 (2020) 217–224.
[25] A. Yonekura, H. Kawanaka, V.B.S. Prasath, B.J. Aronow, H. Takase, Automatic disease stage classification of glioblastoma multiforme histopathological images using deep convolutional neural network, Biomed Eng Lett 8 (2018) 321–327.
[26] J. Fan, J. Wang, Z. Chen, C. Hu, Z. Zhang, W. Hu, Automatic treatment planning based on three-dimensional dose distribution predicted from deep learning technique, Med. Phys. 46 (2019) 370–381.
[27] H. Arabi, H. Zaidi, Applications of artificial intelligence and deep learning in molecular imaging and radiotherapy, Eur. J. Hybrid Imag. 4 (2020) 17.
[28] B. Vanderstraeten, B. Goddeeris, K. Vandecasteele, M. van Eijkeren, C. De Wagter, Y. Lievens, Automated instead of manual treatment planning? A plan comparison based on dose-volume statistics and clinical preference, Int. J. Radiat. Oncol. Biol. Phys. 102 (2018) 443–450.
[29] A.T.Y. Chang, A.W.M. Hung, F.W.K. Cheung, M.C.H. Lee, O.S.H. Chan, H. Philips, Y.T. Cheng, W.T. Ng, Comparison of planning quality and efficiency between conventional and knowledge-based algorithms in nasopharyngeal cancer patients using intensity modulated radiation therapy, Int. J. Radiat. Oncol. Biol. Phys. 95 (2016) 981–990.
[30] J. Krayenbuehl, I. Norton, G. Studer, M. Guckenberger, Evaluation of an automated knowledge based treatment planning system for head and neck, Radiat. Oncol. 10 (2015) 226.
[31] X. Chen, K. Men, Y. Li, J. Yi, J. Dai, A feasibility study on an automated method to generate patient-specific dose distributions for radiotherapy using deep learning, Med. Phys. 46 (2019) 56–64.
[32] A. Akhavanallaf, I. Shiri, H. Arabi, H. Zaidi, Whole-body voxel-based internal dosimetry using deep learning, Eur. J. Nucl. Med. Mol. Imaging 48 (2021) 670–682.
[33] X. Mao, J. Pineau, R. Keyes, S.A. Enger, RapidBrachyDL: rapid radiation dose calculations in brachytherapy via deep learning, Int. J. Radiat. Oncol. Biol. Phys. 108 (2020) 802–812.
[34] L.S. Waters, MCNPX User's Manual, Los Alamos National Laboratory, 2002.
[35] W. Schneider, T. Bortfeld, W. Schlegel, Correlation between CT numbers and tissue parameters needed for Monte Carlo simulations of clinical dose distributions, Phys. Med. Biol. 45 (2000) 459–478.
[36] B. Van Veelen, Y. Ma, L. Beaulieu, Whitepaper: ACE Advanced Collapsed Cone Engine, Elekta Corporation, Veenendal, the Netherlands, 2015.
[37] K. Zourari, E. Pantelis, A. Moutsatsos, L. Sakelliou, E. Georgiou, P. Karaiskos, P. Papagiannis, Dosimetric accuracy of a deterministic radiation transport based (192)Ir brachytherapy treatment planning system. Part III. Comparison to Monte Carlo simulation in voxelized anatomical computational models, Med. Phys. 40 (2013), 011712.
[38] M.J. Berger, Energy deposition in water by photons from point isotropic sources, J. Nucl. Med. (Suppl 1) (1968) 17–25.
[39] J. Seuntjens, W. Strydom, K. Shortt, in: E.B. Podgorsak (Ed.), Dosimetric Principles, Quantities and Units, Radiation Oncology Physics: a Handbook for Teachers and Students, IAEA, Vienna, Austria, 2005.
[40] Y. Murakami, T. Magome, K. Matsumoto, T. Sato, Y. Yoshioka, M. Oguchi, Fully automated dose prediction using generative adversarial networks in prostate cancer patients, PloS One 15 (2020), e0232697.
[41] M.S. Lee, D. Hwang, J.H. Kim, J.S. Lee, Deep-dose: a voxel dose estimation method using deep convolutional neural network for personalized internal dosimetry, Sci. Rep. 9 (2019) 10308.